Hotplate Precipitation Gauge Calibrations and Field Measurements

Nicholas Zelasko [1], Adam Wettlaufer [1], Bujidmaa Borkhuu [1], Matthew Burkhart [1], Leah S. Campbell [2], W. James Steenburgh [2], and Jefferson R. Snider [1, 3]

[1] University of Wyoming Department of Atmospheric Science

[2] University of Utah Department of Atmospheric Sciences

[3] Corresponding Author

Abstract –

First introduced in 2003, approximately 70 Yankee Environmental Systems (YES) hotplate precipitation gauges have been purchased by researchers and operational meteorologists. A version of the YES hotplate is described in Rasmussen et al. (2011; R11). Presented here is indoor- and field-based testing of a newer version of the hotplate; this device is equipped with longwave and shortwave radiation sensors. Hotplate surface temperature, coefficients describing natural and forced convective sensible energy transfer, and radiative properties (longwave emissivity and shortwave reflectance) are reported for two of the new-version YES hotplates. These parameters are applied in a new algorithm, are used to derive liquid-equivalent accumulations (snowfall and rainfall), and these accumulations are compared to values derived by the internal algorithm used in the YES hotplates (hotplate-derived accumulations). In contrast with R11, the new algorithm accounts for radiative terms in a hotplate's energy budget, applies an energy conversion factor which does not differ from a theoretical energy conversion factor, and applies a surface area that is correct for the YES hotplate. Radiative effects are shown to be relatively unimportant for the precipitation events analyzed. In addition, this work documents a 10 % difference between the hotplate-derived and new-algorithm-derived accumulations. This difference seems consistent with R11's application of a hotplate surface area that deviates from the actual surface area of the YES hotplate, and with R11's recommendation for an energy conversion factor that differs from that calculated using thermodynamic theory.

1 - Introduction

Two types of instrumentation are available for making point measurements of liquid-equivalent snowfall rates and liquid-equivalent snow accumulations: 1) Weighing gauges and related devices that measure snowfall as it collects in a container or on a surface (Brock and Richardson, 2001; Chapter 9), and 2) optical gauges that measure the concentration and size of snow particles either in free fall or within a wind tunnel (Loffler-Mang and Joss, 2000; Deshler, 1988). Many of these gauges obstruct the wind and thus cause falling snow particles to deflect from the measurement zone. Consequently, rates and accumulations are underestimated and should be adjusted to account for undercatch (Jevons, 1861; Lovblad et al., 1993). Alternatively, both gauge types can be operated within a fenced enclosure that minimizes wind and the resultant undercatch (Goodison et al., 1998; Rasmussen et al., 2012). In addition, optical gauges require a snow particle density to convert concentration and size to a liquid-equivalent rate and accumulation (Brandes et al., 2007; Lempio et al., 2007). Because this density is variable and difficult to measure accurately (Locatelli and Hobbs, 1974), optical snowfall measurements are uncertain and remain uncertain even if undercatch is accounted for. A further disadvantage, for both the weighing and optical devices, is that the entrance to the device can become clogged with snow (Warnick, 1954; Currie, 1998; Stickel et al., 2005).

The Yankee Environmental Systems (YES, 2011) hotplate was developed to minimize the aforementioned uncertainties. Advantages of the hotplate are: 1) it is compact, 2) it is immune to clogging, 3) there is no requirement that snow particles fall through an opening, and 4) the derived rates and accumulations are largely independent of snow particle density, although a dependence does exist (R11; their figure 14). In some applications, a disadvantage of the

hotplate relative to a weighing gauge, is the hotplate's electrical power consumption. This is ~ 200 W in Wyoming during winter.

This work furthers efforts to advance the hotplate as a snowfall measurement system (Borkhuu, 2009; R11; Boudala et al., 2014). We develop calibration constants for two hotplate systems configured with longwave and shortwave radiation sensors. These are a hotplate gauge owned by the University of Wyoming (UW) and by the National Center for Atmospheric Research (NCAR; Boulder, CO) [1]. In addition, we develop a new hotplate data processing algorithm, derive liquid-equivalent rates and accumulations for 27 precipitation events (snowfall and rainfall), compare accumulations obtained with the new algorithm to those derived by an internal algorithm (hotplate-derived accumulations), and compare accumulations to values derived using weighing gauges.

2 - Algorithm Development

The two stacked circular aluminum plates seen in Fig. 1 are the precipitation measurement portion of the YES hotplate system. The plate diameter (D_h) is 0.130 m and both plates have concentric rings that extend vertically either 3 mm (inner and middle rings) or 1 mm (outer ring) from the plate surface. One of the plates faces upward and is exposed to precipitation, the other faces downward. Temperature sensors monitor the top and bottom plates and feedback-controlled heaters maintain the plates at approximately 75 °C (R11). Electrical power supplied to the top plate (Q_{top}) compensates for power lost via sensible energy, radiative, and vapor mass transfer. Henceforth, we refer to the latter process as latent power output. The hotplate-derived wind speed, evaluated using the "factory calibration" discussed in R11, is used

[1] When a distinction is needed, we indicate the hotplate, followed by a forward slash, and the location of the deployment. For example, the UW hotplate, deployed at the OWL site, is designated UW/OWL.

in this analysis. The bottom plate power (Q_{bot}) is likely a measurement used in the calculation of that wind speed, but this is speculative because the factory wind speed algorithm is proprietary. We symbolize this wind speed as U and use it to evaluate a Reynolds number (Re), and use the latter to parameterize sensible energy transfer from the ventilated surface of the top plate. R11 also derived wind speeds by fitting Q_{bot}, ambient temperature, and a wind speed measured at 10 m above ground level (AGL). This wind speed is not used in this analysis. The hotplate ambient temperature (T) measurement comes from the sensor seen below the radiation instruments (Fig. 1), the relative humidity (RH) measurement comes from a sensor that protrudes below the electronics box (Fig. 1), and the hotplate pressure sensor is contained within the electronics box. A complete description of our nomenclature is provided in the Appendix.

Since the hotplate was introduced in 2003, two teams (Borkhuu, 2009; R11) have reported data processing algorithms. The algorithm in Borkhuu (2009) can be explained by reference to the equation she used to model the top plate's power budget:

$$
\begin{aligned}
0 &= && \text{Implied Steady-state} \\
Q_{top} & && \text{Electrical Power Supplied to Top Plate} \\
- D_h \cdot K_x \cdot (T_h - T) \cdot (\gamma + \alpha \cdot Re^{\beta}) & && \text{Sensible Power Output} \\
- P \cdot E / f_2 & && \text{Latent Power Output} \qquad (1)
\end{aligned}
$$

In Eq. 1, there are three terms that sum to zero in an assumed steady-state. The last of these, the latent power output, is proportional to the precipitation rate (P) and a snow particle catch efficiency (E) and inversely proportional to f_2, an electrical-to-precipitation conversion factor. Also in Eq. 1, the sensible power output has contributions from natural convection (proportional to γ) and forced convection (proportional to $\alpha \cdot Re^{\beta}$), where α, β, and γ are fitted constants. These convective regimes are discussed in Kobus and Wedekind (1995) and are shown graphically in

their Figure 6. Eq. 1 is similar to the algorithm used by King et al. (1978) to derive cloud liquid water concentration using a heated airborne sensor.

The algorithm in R11 is based on Eq. 2.

$$P = [Q_{top} - Q_{bot} - f_1(U)] \cdot f_2 / E \quad (2)$$

Here, $f_1(U)$ is a wind speed-dependent function. Also in Eq. 2, we see the conversion factor introduced in the previous paragraph. Somewhat different from how R11 formulated their conversion factors for rain and snow, we formulate f_2 to account for the warming of ice, melting, warming of the liquid, and liquid evaporation. For rain, we formulate f_2 to account for the warming of liquid and its evaporation. With an exception that we justify later, we applied the conversion factors recommended by R11: 1) if $T < 0$ °C, the snow f_2 is applied, and 2) if $T > 4$ °C the rain f_2 is applied.

In Eq. 1, the sensible power output is a function of *Re*, and thus *U*, and also a function of *T*. Hence, Eq. 1 can be rearranged to look similar to Eq. 2 with *P* dependent on *T*, *U*, Q_{top}, f_2, and *E*. A difference between the Eq. 1 and Eq. 2 formulations is the explicit dependence on Q_{bot}, in Eq. 2; this is in addition to the implicit Q_{bot}-dependent wind speed in *Re* (Eq. 1) and in $f_1(U)$ (Eq. 2).

Borkhuu (2009), YES (2011), and R11 surmised that the energetic effect of longwave and shortwave radiation could, in some settings, be comparable to the latent power output. Consequently, our hotplate (Wolfe and Snider, 2012) was upgraded to firmware version 3.1.2 in 2011. The upgrade included radiation sensors for the measurement of downwelling longwave and shortwave fluxes. An objective of this paper is the incorporation of the radiation measurements into a new precipitation rate algorithm.

We used the following equation to analyze the top plate's power budget:

0 =		Implied Steady-state
Q_{top}		Electrical Power Supplied to Top Plate
$- D_h \cdot K_x \cdot (T_h - T) \cdot (\gamma + \alpha \cdot Re^{\beta})$		Sensible Power Output
$- A_h \cdot \varepsilon_h \cdot \sigma \cdot T_h^4$		Longwave Power Output
$+ A_h \cdot \varepsilon_h \cdot IR_d$		Longwave Power Input
$+ A_h \cdot (1 - R_h) \cdot SW$		Shortwave Power Input
$- P \cdot E / f_2$		Latent Power Output (3)

Compared to Eq. 1, Eq. 3 has three additional terms. These describe the interaction of the top plate with its environment via radiative transfer. Two of these terms are inputs (longwave and shortwave) and one is an output (longwave).

2.1 - Hotplate Data Files

The hotplate outputs data to two files. The previously discussed Q_{top} and Q_{bot} are two of several recorded variables and both of these are essential for the analysis described here. One of the files is known as the UHP or "user" hotplate file. The UHP file is provided to all YES customers. The second file is the SHP or "sensor" file. The SHP file is proprietary but we were granted access to it by NCAR. Table 1 has the list of all recorded variables and how some of these are symbolized. A complete list of variables (measured and computed), and constants, is provided in the Appendix. With the exception of Unix time, all variables in Table 1 are provided as 60-s averages, sampled at 1 Hz (YES, 2011).

2.2 - Radiative Properties

Two radiative properties are applied in our analysis of the top plate's power budget (Eq. 3). In the infrared, or longwave, the emissivity of the top plate is the key property. The material used to fabricate the plates is aluminum, which when exposed to air becomes covered with an aluminum oxide layer. Hence, the hotplate emissivity was taken to be that of oxidized aluminum (ε_h = 0.14; Weast, 1975; Section E). Furthermore, we made two assumptions: 1) the longwave output (Eq. 3) is the product of ε_h, hotplate area (A_h), and the flux emitted by a black body at T_h, and 2) the longwave input (Eq. 3) is the product ε_h, A_h and the downwelling longwave flux (IR_d). In a later section, we explain how we derive IR_d.

In the visible, or shortwave, the top plate's reflectance (R_h) is the key property. Eq. 3 shows how we factored into the power budget the top plate's reflectance, a measured downwelling shortwave flux (SW; Table 1), and A_h. A value for R_h was determined as follows. We exposed the UW hotplate to solar illumination, while measuring the solar flux, and then shaded the hotplate to establish a baseline for the determination of R_h. During these experiments, there was negligible wind and therefore natural convection dominated forced convection in the budget. The budget equation we used to analyze these measurements has three terms: Q_{top}, sensible power output, and solar input. In two experiments, the values R_h = 0.66 and R_h = 0.61 were derived. We apply the average of these (R_h = 0.63) in our analysis of measurements from both UW and NCAR hotplates. Because of the oxide layer, the derived reflectance is smaller than the value reported for polished aluminum reflecting "incandescent" light (0.69; Weast, 1975; Section E) and significantly smaller than the value for vacuum-deposited aluminum at visible wavelengths (0.97; Hass, 1955).

3 - Methods

3.1 Temperature Measurements

Ice bulb temperatures at OWL were calculated using temperature, *RH*, and pressure measurements made within a fully shielded housing (Steenburgh et al., 2014). At GLE and BTL ice bulb temperatures were calculated using the hotplate-derived temperature, *RH*, and pressure values (Table 1). Because the hotplate temperature sensor is incompletely shielded (Fig. 1), there is concern that its measurement is positively biased by solar heating. We investigated this by differencing hotplate-derived temperatures, acquired during precipitation events at OWL, and values acquired by the fully shielded temperature sensor operated at OWL. On average, the hotplate values were larger (0.4 ± 0.4 ^{o}C). We did not attempt to correct for this bias.

3.2 - Site Description

Indoor testing was conducted in a high-bay weather balloon hangar and in a laboratory. These facilities are at the University of Wyoming (UW) and are abbreviated hangar and lab. During wintertime, and especially at night, the hangar is cold (~ 0 ^{o}C); the lab is warm year round (~ 20 ^{o}C). Field measurements (Table 2) were conducted in Southeast Wyoming at the Glacier Lakes Ecosystem Experiments Site (GLE), in Southeast Wyoming near the summit of Battle Pass (BTL), and at the North Redfield site in Western New York (OWL). During both indoor and field measurements, all parameters reported by the hotplate (UHP and SHP variables; section 2.1) were recorded using a custom-built data system.

The accuracy of a hotplate-estimated precipitation rate depends on whether the sensed hydrometeors are rain or snow (R11). We infer the latter using a calculated ice-bulb temperature (T_{IB}) (Iribarne and Godson, 1981; Chapter 7). Measurements used to derive the T_{IB}s are described in section 3.1. The lower limits on these derived values, assuming the measured *RH* is

185 overestimated by 5 % (YES, 2011), is no more than 0.4 ^{o}C colder than the values we report. In
186 instances with T_{IB}s larger than 0 ^{o}C, we assume the sensed hydrometeors were liquid.

187 **3.3 - NOAH-II Gauge**

188 The NOAH-II is a weighing-type gauge manufactured by ETI Instrument Systems Inc.
189 (www.etisensors.com). NCAR operated a NOAH-II at GLE and BTL during 2012, and coauthors
190 (Campbell and Steenburgh) operated a NOAH-II at OWL (Dec. 2013 through Jan. 2014;
191 Campbell et al., 2016). The three NOAH-II gauges were outfitted with Alter shields (Goodison
192 et al., 1998; hereafter G98).

193 **3.4 – Indoor Testing**

194 Indoor testing of the UW hotplate was conducted every year from 2011 to 2015; the
195 NCAR hotplate was only tested in 2012. Based on our testing of the UW hotplate, we have no
196 evidence indicating that the calibration changed over the duration of any of the field
197 deployments; however, Wettlaufer (2013) demonstrates that calibration constants did change
198 over the 2011 to 2015 interval, and likely in response to servicing conducted twice at YES. In
199 this paper we present calibration constants appropriate for the UW hotplate sensor deployed at
200 GLE (April 2012) and at OWL (December 2013 through January 2014).

201 During testing, we controlled the hotplate's radiation environment by placing a material
202 with known emissivity (painted-steel sheeting, $\varepsilon_s = 0.84$) above and below the hotplate. The steel
203 sheets were positioned to dominate the hotplate's upward and downward fields of view (Fig. 2);
204 however, the sheets were positioned so that they were not heated by the hotplate. In that case, the
205 sheet temperature (T_s) can be assumed equal to T.
206

3.5 - Downwelling Longwave Flux

As we have already mentioned, previous work concluded that the hotplate method of determining precipitation can be affected by longwave radiation. In response to that finding, newer versions of the hotplate have a device that measures longwave radiation (pyrgeometer, e.g., Albrecht et al., 1974) (Fig. 1 and Table 1).

$$M_{IR} = IR_d - IR_u \quad (4)$$

The left-hand side of Eq. 4 represents the longwave measurement (M_{IR}) and the right-hand side has the downwelling and upwelling components contributing to M_{IR}.

Because IR_d appears in the top plate's power budget (Eq. 3), and since M_{IR} is the only term in Eq. 4 that is measured, the upwelling component (IR_u) must be evaluated. This is possible because the signal from the pyrgeometer is adjusted, within the hotplate electronics package, to make the source of the upwelling flux a virtual blackbody at the ambient temperature (YES 2012, personal communication). In that case, IR_d can be formulated as

$$IR_d = M_{IR} + \sigma \cdot T^4 \quad (5)$$

where σ is the Stefan-Boltzmann constant and T is the hotplate-measured ambient temperature. We also use Eq. 6 to calculate the downwelling longwave flux

$$IR_d = \varepsilon_s \cdot \sigma \cdot T_s^4 \quad (6)$$

3.6 – Warm-Cold Ambient Temperature Tests

Procedures described here were applied during testing conducted indoors (hangar and lab, section 3.2) at two different temperatures and are hereafter referred to as the warm/cold test. We show how values of a warm (T_w) and cold (T_c) ambient temperature, combined with other

229 recorded hotplate variables (Table 1), can be used to derive two calibration parameters in Eq. 3
230 (T_h and γ). In our analysis, the temperature of the steel sheeting (T_s) was assumed equal to the
231 ambient temperature (either T_w or T_c) and IR_d was calculated using Eq. 6. By design these tests
232 had negligible forced-convective and latent energy transfers. In that case, Eq. 7a - b are the top
233 plate budget equations.

234 $$0 = Q_{top,w} - D_h \cdot K_x \cdot (T_h - T_w) \cdot \gamma - A_h \cdot \varepsilon_h \cdot \sigma \cdot T_h^4 + A_h \cdot \varepsilon_h \cdot \varepsilon_s \cdot \sigma \cdot T_w^4 + A_h \cdot (1 - R_h) \cdot SW_w \quad (7a)$$

235 $$0 = Q_{top,c} - D_h \cdot K_x \cdot (T_h - T_c) \cdot \gamma - A_h \cdot \varepsilon_h \cdot \sigma \cdot T_h^4 + A_h \cdot \varepsilon_h \cdot \varepsilon_s \cdot \sigma \cdot T_c^4 + A_h \cdot (1 - R_h) \cdot SW_c \quad (7b)$$

236 The measurements applied in these equations were T_w and T_c, the warm and cold plate powers
237 ($Q_{top,w}$ and $Q_{top,c}$), the warm and cold shortwave fluxes (SW_w and SW_c), and constants
238 (Appendix). Values of T_h and γ (hereafter referred to as T_h/γ pairs) were derived by minimizing
239 departures from zero simultaneously in Eq. 7a - b. Minimization was conducted using a
240 Newton's method equation solver (Exelis Visual Information Solutions, Inc.); the convergence
241 tolerance was 1×10^{-4} J s^{-1}.

242 **3.7 - Nusselt-Reynolds Relationship**

243 The Nusselt number ($Nu = \gamma + \alpha \cdot Re^{\beta}$), is a component of the sensible power output term
244 in Eq. 3. In this section, we develop a relationship between *Nu* and *Re* based on
245 measurements recorded in the field when precipitation was not occurring; in a later section
246 we show how that relationship was applied in the new algorithm.

247 Conceptually, *Nu* is a dimensionless representation of the sensible power output. Eq. 8a
248 was used to calculate *Nu* with measurements (Q_{top}, *T*, and *SW*), a calculated variable (IR_d; section
249 3.5), and constants (Appendix and Table 3).

250 $$Nu = [Q_{top} - A_h \cdot \varepsilon_h \cdot \sigma \cdot T_h^4 + A_h \cdot \varepsilon_h \cdot IR_d + A_h \cdot (1 - R_h) \cdot SW] / [D_h \cdot K_x \cdot (T_h - T)] \quad (8a)$$

In the numerator are the terms contributing to the sensible power output, and in the denominator is a term proportional to the sensible power due to molecular conduction.

Conceptually, *Re* is a dimensionless representation of the wind speed. Eq. 8b was used to calculate *Re* with a measurement (*U*) and constants (Appendix).

$$Re = p_x \cdot D_h \cdot U / (R_d \cdot T_x \cdot \mu_x) \quad (8b)$$

Two criteria were used to select a site-specific data subset for the *Nu*-*Re* development: 1) no precipitation, and 2) at least three hours of continuous measurements with a broad range of wind speeds. We fitted the selected *Nu*-*Re* pairs using a non-linear least squares procedure (curvefit; Exelis Visual Information Solutions, Inc.); the convergence tolerance for the relative decrease in chi-squared was 1×10^{-3}.

3.8 - Electrical-to-precipitation Conversion Factor

Equilibrium thermodynamics, with the assumptions that ice melts at $T_o = 0$ °C and vaporization occurs at T_h, was used to derive the conversion factor in Eq. 3 (f_2). Adopting the temperature criteria from R11 (also see section 2), and a framework from Iribarne and Godson (1981; Chapter 7), we formulated the theoretical conversion factors as

$$f_2(T, T_h) = \{\rho \cdot A_h \cdot [\, C_i \cdot (T_o - T) + L_f(T_o) + C \cdot (T_h - T_o) + L_v(T_h)]\}^{-1} \quad (T < 0\ ^oC) \quad (9a)$$

$$f_2(T, T_h) = \{\rho \cdot A_h \cdot [\, C \cdot (T_h - T) + L_v(T_h)]\}^{-1} \quad (T > 4\ ^oC) \quad (9b)$$

This formulation is graphed in Fig. 3a (solid line) where we extended Eq. 9b into the temperature range (0 °C < T < 4 °C) where the distinction between rain and snow is ambiguous (R11).

We now compare the conversion factor derived using Eq. 9a – b with that reported in R11. To be consistent with R11, we assume $T = T_h = 0$ °C. We find that the ratio of f_2 (Eq. 9a) divided by the factor reported in R11 for snow (3.99×10^{-8} m J^{-1}) and the ratio of f_2 (Eq. 9b)

divided by the factor reported in R11 for rain (4.52×10^{-8} m J^{-1}), are both 0.666. Since these ratios are equal to the area in R11 ($A_h = 0.008844$ m^2), divided by the area applied in our calculation ($A_h = (\pi/4)\cdot 0.130^2 = 0.01327$ m^2), we conclude that the discrepancy is not due to differing thermodynamic parameters applied in R11's and our calculations (e.g., the latent heat of vaporization), rather it stems from the different values used for the hotplate area. Further, R11 changed their theoretical f_2 to an actual conversion factor that was "..lower because of the imperfect heat transfer from the precipitation to the hot plate (losses to the air, e.g.)." We do not find justification for this in R11, nor do we agree with R11's assignment of $A_h = 0.008844$ m^2 assuming they were recommending that value for the hotplate sold by YES. Recently, Boudala et al. (2014) addressed the second of these two points, making it clear that $A_h = 0.01327$ m^2 is appropriate for the hotplate sold by YES.

In light of the above, the ratio of our f_2 (Eq. 9a – b with $T = T_h = 0$ °C), divided by the actual conversion factor in R11, is 0.86 for snow and 0.89 for rain. Since a derived precipitation rate is proportional to f_2 (e.g., Eq. 2), we expect the ratio of a precipitation rate from the new algorithm (assuming $T = T_h = 0$ °C), divided by a synchronous hotplate-derived precipitation rate, to be between 0.86 and 0.89. Our expectation hinges on the assumption that the YES algorithm has incorporated R11's surface area and R11's distinction between theoretical and actual conversion factors.

We calculate f_2 in the new algorithm two ways: 1) In a comparison made to a hotplate-derived accumulation, our f_2 is set to 2.66×10^{-8} m J^{-1} (snow) and 3.01×10^{-8} m J^{-1} (rain). These values were obtained from Eq. 9a – b with $T = T_h = 0$ °C and are displayed as a dotted line in Fig. 3a. 2) In comparisons made to either a NOAH-II accumulation or to a laboratory reference precipitation rate, we evaluate f_2 using Eq. 9a – b with a T_h from Table 3 and with the hotplate-

measured ambient T (Table 1). In addition to the step change due to the difference between the latent heats of sublimation and vaporization, our conversion factor has a weak temperature dependence (Fig. 3a, solid line). This is due to the warming discussed in section 2. Also, in Fig. 3a we display the actual conversion factor from R11 (dashed line). Our classification of measurements into snow and rain is discussed in a later section.

3.9 – Snow Particle Catch Efficiency

In this section, we evaluate a wind speed-dependent function and use it to account for the top plate's snow particle catch efficiency (E; section 2). The physical processes this function accounts for are, 1) snow particle bouncing subsequent to collision with the top plate, followed by transfer away from the top plate by wind, and 2) shearing off of a snow particle after it has landed on the top plate (R11). This conceptual description of catch on the hotplate is different from that used to describe catch by weighing gauges where undercatch results because a subset of snow particles are carried over the gauge by a vertically-accelerated flow (Nespor and Servuk, 1999; Thériault et al., 2012). Both R11 and G98 derive catch efficiencies as the ratio of two paired values of liquid-equivalent accumulation, one obtained from the gauge of interest and the other obtained from a second gauge operated inside a Double Fence Intercomparison Reference Shield (DFIR).

The snow particle catch efficiency functions applied here are both gauge- and location-specific. For the UW hotplate (at GLE and OWL), and the NCAR hotplate (at BTL), we apply the function recommended by YES (YES 2012, personal communication; hereafter Y12). Wind speeds used in the efficiency calculation are the hotplate-derived U. In addition, the hotplate catch efficiency function described by R11 (their Equation 6) was also applied. This was based on the hotplate U adjusted to the 10-m level with a roughness length z_o = 0.3 m (G98, their

Equation 4.3.1) and was only used in analysis of measurements made at OWL. The z_o we picked corresponds to a surface with "Many trees, hedges, few buildings" (Panofsky and Dutton, 1984; their Table 6.2). This assignment is consistent with the presence of shrubs and trees (Steenburgh et al., 2014), and a two-story barn, at the OWL site. The barn was located at the eastern edge of a fallow field, 80 m west of the gauges at OWL. For the NOAH-II gauge, we applied a function developed for an 8-inch (diameter) Alter-shielded gauge (G98; their Equation 4.7.1). Wind speeds used in that calculation are from the hotplate (at GLE and BTL) or from an anemometer (at OWL) (Campbell et al., 2016). Of course, we are assuming that the function from G98 mimics undercatch by our 12-inch (diameter) Alter-shielded NOAH-II gauge.

In Fig. 3b, we present the three catch efficiency functions (R11 with U adjusted to 10 m, Y12, and G98). In this graph, the wind speed applied in the R11 function is the value plotted on the abscissa multiplied by 2.9. This adjustment corresponds to the lowest installation of the hotplate at OWL and decreases to 2.0 for measurements made after 20131217 [2]. In our calculation of the R11 catch efficiency functions, the snow depth for the interval of interest (20131211 to 20140129) was set equal to the average (0.7 m) derived using an ultrasonic snow depth instrument operated at OWL (Campbell et al., 2016). This average, and the AGL altitudes of the hotplate installation (Table 2), were used to derive the two wind-speed adjustment factors (2.9 and 2.0). The basis for this calculation is G98's gauge-height correction formula (their Equation 4.3.1).

Since the anemometer at OWL was operated at nearly the same height as the top of the NOAH-II gauge (Steenburgh et al., 2014), and the G98 catch efficiency formula (their Equation

[2] AGL altitudes of the two hotplate installations are provided in Table 2.

340 4.7.1) assumes speeds are measured at the height of the gauge opening, a vertical adjustment of
341 the wind speed was not factored into the G98 catch efficiencies.

342 **4 – Testing and Calibration Results**

343 **4.1 – Warm-Cold Tests**

344 Results from the warm-cold tests are described here. The derived T_h/γ pairs (section 3.6)
345 are in Table 3. The T_h values are 42.2 ^{o}C for the NCAR hotplate deployed at BTL (NCAR/BTL),
346 52.2 ^{o}C the UW hotplate deployed at (UW/GLE), and 65.5 ^{o}C for the UW gauge deployed at
347 OWL (UW/OWL). The first two T_hs differ from those presented in Wettlaufer (2013) where, for
348 the NCAR hotplate, he reported agreement with the nominal plate temperature (75 ^{o}C; R11) and
349 for the UW hotplate (GLE) he reported a larger temperature (T_h = 109 ^{o}C). The T_h/γ pair
350 reported in Table 3, for the UW/OWL study, was evaluated after Wettlaufer (2013) reported his
351 warm-cold test results.

352 In our analysis of the warm-cold measurements we only used data acquired in the hangar.
353 As we describe below, this may have improved the accuracy of the resultant T_h/γ pairs. This is
354 because all data needed to derive a T_h/γ pair can be obtained without turning off the hotplate.
355 Wettlaufer (2013) analyzed both hanger and lab data. Both in his work and in ours, the relevant
356 hotplate properties were derived by averaging over a 5 minute warm interval and a 5 minute cold
357 interval, and applying these averages in Eq. 7a – b. For us the warm-cold temperature pairings
358 are 5.4/-4.3 °C (NCAR/BTL), 7.0/-1.1 °C (UW/GLE), and 29.5/10.4 °C (UW/OWL). Compared
359 to Wettlaufer (2013), our T_ws are 15 °C colder (NCAR/BTL and UW/GLE experiments only).
360 Using our T_h/γ pairs (Table 3) and the first two T_ws (i.e., for NCAR/BTL and UW/GLE), we
361 evaluated the term in Eq. 7a representing natural-convective transfer ($D_h \cdot K_x \cdot (T_h - T_w) \cdot \gamma$) and

362 compared to values derived using T_h/γ pairs in Wettlaufer (2013; his Table 2). In the NCAR/BTL
363 comparison T_w was set at 5.4 °C and in the UW/GLE comparison T_w was set at 7.0 °C. Our
364 natural-convective term agrees within ± 0.1 W of those derived by Wettlaufer (2013). Also in
365 good agreement is the product of T_h and γ. Relative to Wettlaufer (2013), our $T_h \times \gamma$ product is 6
366 % larger (NCAR/BTL), and 7 % larger (UW/GLE). We expect that our T_h/γ pairs (Table 3),
367 when applied in Eq. 3, will produce a reasonable estimate of the precipitation rate. We test that
368 expectation in the next section.

369 Error limits on T_h and γ, in Table 3, were derived by perturbing $Q_{top,w}$ (i.e., the value
370 acquired in the warm test) by ± 0.5 W and repeating the analysis (Eq. 7a - b). Our estimate of the
371 $Q_{top,w}$ error (± 0.5 W) came from a comparison of values acquired before and after power to the
372 hotplate was stopped and restarted. These tests were conducted in the hangar and the 10 min
373 warm up recommended by the manufacturer was adhered to (YES, 2011).

374 **4.2 - Drip Tests**

375 This section compares two time sequences of precipitation rate: one calculated with the
376 new algorithm, the other is the hotplate-derived value (Table 1). The basis for the comparison is
377 measurements of artificially-produced liquid precipitation made in the hangar. We applied water
378 drops to the NCAR and UW hotplates using a volumetric water pump (Ismatec Inc.; Model
379 7618). Each of these tests has a drip period (4 min) and a nondrip period (5 min). Drops (4 mm
380 volume-equivalent diameter) were added uniformly to the top plate at a constant volumetric rate.
381 We convert the pump rate to a reference precipitation rate (P_{REF}) and apply the P_{REF} in
382 subsequent analyses [3]. These drip tests were conducted at $T > 4$ °C.

[3] The value of the multiplier that converts the volumetric pump rate ($cm^3\ min^{-1}$) to precipitation rate ($mm\ hr^{-1}$) is 4.51.

Because the drip tests were conducted with the hotplate operating as in Fig. 2, and unventilated, the recorded data were analyzed with $T_s = T$, in Eq. 6 (section 3.5), and with the sensible power output formulated as $D_h \cdot K_x \cdot (T_h - T) \cdot \gamma$ (Appendix and Table 3). Also, because all of the pumped water is delivered to the top plate, the catch efficiency is $E = 1$. Hotplate precipitation rates were derived by inputting measurements (Q_{top}, T, U, and SW) and a calculated variable (IR_d; section 3.5) into Eq. 3 and solving for a precipitation rate sequence ($P(t)$). We symbolize this $P(t)$ as P_{UW} and refer to calculations leading to that sequence as the UW algorithm. Also, we refer to sequences obtained from the UHP file (Table 1) as P_{YES} and refer to that calculation as the YES algorithm.

We now compare values of P_{UW} to synchronous values of P_{YES}. Typically, these rates exhibit a maximum ~ 3 min after the nondrip-to-drip transition (Fig. 4). We interpret these maxima as overestimates, possibly due to a violation of the steady-state assumption. Also evident, particularly in the P_{UW} sequence, is a minimum. This occurs during the time the instrument is relaxing to its rest state; i.e. ~ 2 min after a drip-to-nondrip transition. The figure also demonstrates that thresholding is applied to the P_{YES} sequence, i.e. the YES algorithm thresholds the output to 0 mm hr^{-1} if values decrease to < 0 mm hr^{-1}. This is evident at ~ 16:11 UTC and at three other times in the P_{YES} sequence. In fact, thresholding is not desired for the drip tests. Thus, the UW sequence is not thresholded in Fig. 4.

Two 1-min averaging intervals are shown in Fig. 4. We set the end of these at the drip-to-nondrip transitions and symbolize the averages as $\langle P_{UW} \rangle$ and $\langle P_{YES} \rangle$. Fig. 5 is a compilation of the two tests already discussed plus four additional P_{REF} vs $\langle P_{UW} \rangle$ comparisons and four additional P_{REF} vs $\langle P_{YES} \rangle$ comparisons.

We now use linear least-squares regression analysis, and a regression equation of form $y = a \cdot x$, to derive the ratio of two precipitation rates. In Fig. 5 it is apparent that the regression slope (ratio), derived for the P_{REF} vs $<P_{UW}>$ comparison, does not differ from one by more than ± 1 standard deviation. Ratios for the two hotplates (UW and NCAR) and for three drip tests are summarized in Table 4. In the third column (P_{REF} vs $<P_{UW}>$), we see that none of the ratios differ from one by more than ± 1 standard deviation. Different from Fig. 5 and Table 4, we also evaluated intercepts of regressions that were not forced through the origin; none of these intercepts differ significantly from zero (results not shown). From the statistical comparisons in Table 4, we conclude the T_h/γ pairs (Table 3) applied in the UW algorithm (Eq. 3) produce a precipitation rate consistent with the reference.

Values of the reference rate and the hotplate-derived rate ($<P_{YES}>$) are compared as ratios in Fig. 5 and in the fourth column of Table 4. These ratios are seen to deviate systematically from unity, and in the direction discussed in section 3.8. In the unforced regressions (not shown) the intercepts are negative, but only one of these differed significantly from zero (NCAR/BTL; intercept = -0.3 ± 0.1). Negative intercepts are expected because P_{YES} is positively offset, by ~ 0.2 mm hr^{-1}, during most of the nondrip periods (e.g., 16:21 UTC in Fig. 4).

5 - Field Measurements

This section is organized as follows: Section 5.1 presents field measurements of ambient temperature and ambient ice-bulb temperature. We use this information to classify 27 precipitation events as snowfall or rainfall. Section 5.2 presents the *Nu-Re* relationship we use to account for the sensible power output in Eq. 3. Section 5.3 describes how we derive a precipitation rate for a hotplate based on measurements made in the field. Section 5.4 compares

427 time-integrated precipitation rates (accumulations) derived using the two algorithms. In section
428 5.4, we also compare hotplate accumulations to values from the NOAH-II.
429

5.1 – Field-measured Temperatures and Ice-bulb Temperatures

The 27 precipitation events are summarized in Table 5. Measurements were made during 2012, at the two Southeast Wyoming field sites (BTL and GLE), and during 2013 and 2014 at the Western New York site (OWL). Table 5 and Fig. 6 have event-averaged ambient temperatures ($<T>$) and event-averaged ambient ice-bulb temperatures ($<T_{IB}>$). Twenty-three of the events have $<T> \leq -3.3$ ^{o}C and upper-limit temperature ($<T>$ plus two standard deviations) no warmer than -2.3 ^{o}C. We classified these as snowfall. In addition, we classified four events as rainfall. These had $<T_{IB}> \geq +2.9$ ^{o}C and lower-limit temperature ($<T>$ minus two standard deviations) no colder than +2 ^{o}C.

5.2 - Nusselt-Reynolds Relationship

Fig. 7b shows a plot of the *Nu*-*Re* fit function with the data used to constrain the function. This result is based on UW hotplate measurements (GLE site) and formulas developed in section 3.7. Fit coefficients (α, β, and γ) are reported in Table 6 for each field site. Hansen and Webb (1992) reported $\alpha = 0.09$ and a β between 0.69 and 0.72 for a surface similar to the hotplate (circular with three concentric rings); however, their flow direction was perpendicular to the plate surface. The values of α and β we report may differ from those in Hansen and Webb (1992) because the flow is principally parallel to the plate surface at our field sites. There are two other differences relative to Hansen and Webb (1992): 1) Our geometrically-averaged *Nu* (~ 360) is about a factor of five larger, and 2) our *Re* extends over a much larger range. Finally, we note that compared to Fig. 7b there is an order of magnitude narrower *Re* range in the NCAR/BTL and UW/OWL *Nu*-*Re* plots (not shown).

Fig. 7a is a companion to Fig. 7b showing the γ based on the warm-cold test. The error limit on this datum is explained in section 4.1. Since *Nu* is dependent on the T_h derived in the warm-cold test (section 3.6), we expect the *Nu*-*Re* function to converge to the warm-cold γ in the limit of small *Re*. In our assessment of convergence, we evaluated the limiting *Nu* at the *Re* corresponding to the minimum *U* reported in the hotplate data output (0.1 m s^{-1}). This minimum *U* establishes the left end of the function in Fig. 7b. Convergence of the *Nu*-*Re* relationship to within the error limit on the warm-cold γ, at the former's left-most limit, is evident in Fig. 7a – b. Convergence is also evident in the NCAR/BTL and UW/OWL plots analogous to Fig. 7a – b (not shown) and this in spite of narrower *Re* range in those datasets.

5.3 - Precipitation Rate from Field Measurements

Fig. 8 shows budget terms (Eq. 3) for one of the four rainfall events in our dataset (OWL-15). The three output terms (sensible, latent, and longwave), and three input terms (top plate, longwave, and shortwave) are shown in Fig. 8a - b. In this section we begin with the latent power output (i.e., $P \cdot E/f_2$ in Fig. 8a) and describe how we calculate the rainfall rate. We also contrast that calculation with steps followed in the case of snowfall.

The first step in the calculation is conversion of the latent power output term (Fig. 8a) to a provisional precipitation rate; this is done by multiplying each element of the term by the corresponding element of f_2 (Eq. 9b). This operation is referred to as element-by-element vector multiplication. Thresholding is applied next. Both a 300-s running average of the provisional rate and a 10-s running average of the provisional rate are computed. If the 300-s average exceeds 0.25 mm hr^{-1}, and the 10-s average exceeds 0 mm hr^{-1}, the rate is stored as the 10-s average; otherwise the rate is stored as 0 mm hr^{-1}. We refer to the resultant as P_{UW}, but we note that in section 4.2 the P_{UW} sequences are unthresholded. Both the thresholded and unthresholded

sequences are presented in Fig. 8c – d. The thresholded P_{UW} is identical to the unthresholded P_{UW} where the 300-s average exceeds 0.25 mm hr^{-1} and the 10-s average exceeds 0 mm hr^{-1}.

In the case of snowfall, the f_2 is calculated using Eq. 9a and applied as discussed in the previous paragraph. Finally, the precipitation rate is derived as the resultant of element-by-element vector multiplication of the thresholded P_{UW} and the reciprocal of the snow particle catch efficiency (section 3.9).

5.4 – Comparisons of Liquid-equivalent Accumulation

Here we use linear least-squares regression analysis, with a regression equation of form $y = a \cdot x$, to derive the ratio of two measures of liquid-equivalent accumulation for snow. In Fig. 9, these measures are the accumulations derived using the UW and YES algorithms. In the these algorithms the particle catch efficiency function is the one described in Y12 and f_2 is 2.66×10^{-8} m J^{-1} (section 3.8). The data points correspond to measurements made at GLE (UW hotplate), at BTL (NCAR hotplate), and at OWL (UW hotplate). We note that 19 of 23 *y*-axis values are from the same instrument (UW hotplate) and are derived using the same calibration (UW/OWL) used to produce the result shown in the third row of Table 4. Statistical consistency between the ratio in Fig. 9 (0.79 ± 0.05) and the ratio in the third row of Table 4 (i.e., 0.79 ± 0.03 for the P_{REF} vs $\langle P_{YES} \rangle$ ratio) suggest a systematic error in the YES-derived precipitation rates and accumulations. This assertion is reinforced by the three NCAR hotplate points straddling the best-fit line, in Fig. 9, and by the ratio reported in Table 4 for the NCAR hotplate (i.e., 0.81 ± 0.03 for the P_{REF} on $\langle P_{YES} \rangle$ ratio). However, we cannot exclude the possibility that bias in our field-based calibration coefficients (α, β, and γ; Table 6) is the reason for a UW/YES ratio significantly smaller than unity in Fig. 9.

As was discussed in section 4.2, and demonstrated in Fig. 4, during the indoor nondrip periods the P_{YES} sequence is positively offset. A plausible reason for this, and for the ratios < 1 reported in the previous paragraph, is disregard for longwave forcing in the YES algorithm. Since we do not have access to the YES algorithm, we estimated the longwave radiative effect by setting the longwave terms to zero in Eq. 3. After doing this, a larger UW/YES ratio (a = 0.83 ± 0.04) was obtained in a plot analogous to Fig. 9. From this modest increase of the UW/YES ratio, we conclude that longwave forcing *cannot* explain the shift of the best-fit line away from unity in Fig. 9. An even smaller perturbation of the UW/YES ratio was obtained in calculations that set the shortwave term to zero in Eq. 3 (results not shown).

Further evidence for systematic error in the YES values comes from Fig. 10. With the exception that these data are for rain observed at OWL (section 5.1) the comparison in Fig. 10 is similar to Fig. 9. Although the number of points is small, Fig. 10 establishes that our finding of a UW/YES ratio significantly smaller than unity is true for both rainfall and snowfall. In addition, Fig. 11 strengthens this conclusion by showing agreement between values of the UW accumulation and the NOAH-II accumulation when both gauges detected rain.

An additional assessment of snowfall at OWL is presented in Fig. 12a – c. In these graphs the NOAH-II measurements are plotted on the abscissa and different interpretations of the UW hotplate measurements are plotted on the ordinate. For both devices, we plot the ratio of a liquid-equivalent accumulation divided by an event-averaged catch efficiency, and we note that the numerator of these ratios are accumulations that were not corrected for inefficient catch [4]. Table 5 demonstrates two features of the OWL snow data set: 1) The event-averaged catch efficiency based on Y12 (<*E Y12*>) is consistently larger than the event-averaged efficiency based on R11

[4] This comparison was also made using accumulations corrected with a time-dependent catch efficiency (section 5.3), but we found that the fit-line slopes differed by less than ± 5 % from those in Fig. 12.

519 (<*E R11*>), and 2) the event-averaged efficiency <*E R11*> is comparable to <*E Y12 An*>, where
520 the latter is the event-averaged efficiency derived with the anemometer *U* and the Y12 catch
521 efficiency function. These features are consistent with the altitude adjustment in R11, which
522 increases the wind speed (section 3.9), and thus decreases <*E R11*> relative to <*E Y12*>. They
523 are also consistent with a low bias in the hotplate-derived *U*. The latter is supported by a
524 comparison of the hotplate *U* vs anemometer *U* where the fit-line slope is 0.55 ± 0.05 for the 19
525 snow events at OWL (results not shown).
526 Consistent with the ranking of event-averaged values of *E* (Table 5), Fig. 12a shows that
527 the hotplate values, derived with the hotplate *U* and the Y12 catch efficiency function, are
528 smaller (on average) than the NOAH-II-derived values. We also see that the 15% underestimate
529 in the hotplate (Fig. 12a) reverses to a slight overestimate when using the R11 catch efficiency
530 function (Fig. 12b) and when using the anemometer *U* with the Y12 function (Fig. 12c). These
531 results do not allow us to specify contributions to the 15% underestimate (Fig. 12a), coming
532 from the fact that the Y12 function does not use a height-adjusted *U*, or from the suspected
533 hotplate underestimate of *U*. Further studies focused on development of a hotplate catch
534 efficiency function dependent on the local wind speed, as opposed to the wind speed at 10 m
535 (R11), and investigation of the hotplate's determination of wind speed, are needed to resolve this
536 issue. Since there is error in the NOAH-II values used in this comparison, there is also need for
537 characterization of that uncertainty (random and systematic). Error can propagate from the
538 NOAH-II measurements themselves and from the catch efficiency function we applied to those
539 data (section 3.9).
540

6 - Conclusions

Starting with measurements acquired from two YES hotplates, we derived precipitation rates and accumulations for 27 snowfall and rainfall events. The basis for this is a power budget equation similar to that in King et al. (1978). We changed the budget equation by including terms describing the longwave and shortwave radiant energy transfers. To the best of our knowledge, this is the first time that radiative terms have been incorporated into a hotplate data analysis algorithm and reported in the scientific literature.

We demonstrated that radiative forcing of the budget is relatively unimportant for the precipitation events analyzed. This is because the top plate's shortwave absorptance (i.e., $1 - R_h$ in Eq. 3), and its longwave emissivity, are small compared to unity, because a majority of events occurred at night, and because generally overcast conditions diminished the significance of the longwave forcing.

In this paper, we used computational methods different from those in R11, and we derived and applied different calibration coefficients. In spite of these changes we report precipitation rates and accumulations that strongly correlate with the output of two YES hotplates. However, a systematic difference is evident in our comparisons of the UW and YES algorithms. We surmise that the difference comes from the following: 1) R11's assignment of A_h (0.00884 m^2 vs 0.01327 m^2 in the UW algorithm), 2) R11's distinction between a theoretical and an actual energy conversion factor, and 3) the incorporation of #1 and #2 into the YES algorithm. Clearly, R11's A_h is not justified for hotplates sold by YES (Boudala et al., 2014; YES 2017, personal communication). R11's distinction between conversion factors is more problematic. That distinction can be interpreted two ways: either 1) The distinction accounts for

environmental thermal energy input that assists the conversion of precipitation mass to vapor, or 2) the distinction accounts for the loss of snow particles from the top surface of the hotplate due to removal by wind. Because early in the warming process a precipitation element attains a temperature larger than that of the air, we assert that the first of these phenomena is unlikely to contribute significantly to the energy budget. The second may be significant, but it is our opinion that removal of precipitation mass by wind is best accounted with a catch efficiency, not with a distinction between conversion factors. Lastly, accounting for either of these phenomena, independent of an adjustment of the catch efficiency, should be accomplished with an increase of an actual conversion factor relative to the theoretical value, not with the decrease proposed by R11.

Acknowledgements -

We gratefully acknowledge the support provided by the UW Department of Atmospheric Science Engineering Group. We also thank Ontario Winter Lake-effect Systems (OWLeS) project PIs Bart Geerts and Dave Kristovich for their leadership and Philip Bergmaier for maintaining the UW hotplate during OWLeS. This work was supported by the United States National Science Foundation (Award EPS 1208909), the Wyoming Water Development Commission (Award WWDC40395H), and by the U.S. Department of Interior (Award 1000628L).

Appendix – Nomenclature

A_h	Area of YES hotplate = 0.01327 m^2
C	Liquid H_2O specific heat capacity = 4218 J kg^{-1} K^{-1} (assumed independent of temperature; Iribarne and Godson, 1981; their Table IV-5)
C_i	Solid H_2O specific heat capacity = 2106 J kg^{-1} K^{-1} (assumed independent of temperature; Iribarne and Godson, 1981; their Table IV-5)
D_h	Diameter of YES hotplate = 0.130 m
E	Snow particle catch efficiency (section 3.9)
f_1	Wind speed-dependent property in Eq. 2 [W]
f_2	Electrical-to-precipitation conversion factor [m J^{-1}]
IR	Upwelling or downwelling component of longwave flux [W m^{-2}]
$L_f(T_o)$	Latent heat of fusion evaluated at the thermodynamic reference temperature = 0.3337×10^6 J kg^{-1} (Iribarne and Godson, 1981; their Table IV-5)
$L_v(T_h)$	Latent heat of vaporization at T_h (Iribarne and Godson, 1981; their Equation 4.103) [J kg^{-1}]
M_{IR}	Measured longwave flux (section 3.5) [W m^{-2}]
Nu	Nusselt number
P	Liquid-equivalent precipitation rate [mm hr^{-1} or m^3 m^{-2} s^{-1}]
P_{Ref}	Reference precipitation rate (section 4.2) [mm hr^{-1} or m^3 m^{-2} s^{-1}]
P_{UW}	Precipitation rate derived with UW algorithm (section 5.3) [mm hr^{-1} or m^3 m^{-2} s^{-1}]
P_{YES}	Precipitation rate derived with YES algorithm (section 4.2) [mm hr^{-1} or m^3 m^{-2} s^{-1}]
Q_{bot}	Bottom plate power [W]
Q_{top}	Top plate power [W]
R_d	Dry air specific gas constant = 287 J kg^{-1} K^{-1}
Re	Reynolds number
R_h	Hotplate Reflectance = 0.63 (section 2.2)
SW	Measured shortwave flux (section 2.2) [W m^{-2}]
T	Ambient temperature [^{o}C or K]
T_h	Hotplate surface temperature (section 3.6) [^{o}C or K]
T_o	Thermodynamic reference temperature = 0.0 ^{o}C
T_s	Temperature of painted-steel sheeting [^{o}C or K]

U	Wind speed [m s^{-1}]

Greek Symbols

α	Fitted *Nu-Re* Coefficient (section 3.7)
β	Fitted *Nu-Re* Coefficient (section 3.7)
ε_h	Hotplate emissivity = 0.14 (section 2.2)
ε_s	Emissivity of painted-steel sheeting = 0.84 (section 3.4)
γ	Coefficient derived in warm-cold tests (section 3.6) or a coefficient in the *Nu-Re* relationship (section 5.2)
ρ	Liquid H_2O density = 1000 kg m^{-3} (assumed independent of temperature)
σ	Stefan-Boltzmann constant = 5.67x10^{-8} W m^{-2} K^{-4}

Subscripts

c	Indoor cold setting
d	Downwelling
h	Hotplate
IB	Ice-bulb
s	Painted-steel sheeting
u	Upwelling
w	Indoor warm setting
x	Property of air film adjacent to the hotplate surface: p_x = standard-atmosphere pressure at the altitude of the measurement. The following three film properties are held constant in calculation of the Reynolds number (section 3.7) and in calculation of the sensible power output due to molecular conduction (section 3.7): 1) temperature (T_x = 303.15 K), 2) dynamic viscosity (μ_x = 1.862x10^{-5} kg m^{-1} s^{-1}; Rogers and Yau (1989; their Table 7.1)), and 3) thermal conductivity (K_x = 2.63x10^{-2} J m^{-1} s^{-1} $K^{-1;}$ Rogers and Yau (1989; their Table 7.1)).

640

641 **Operator**

642 $\langle y \rangle$ Time average of property y

643

References

Albrecht, B., M. Poellot, and S.K. Cox, Pyrgeometer measurements from aircraft, Review of Scientific Instruments, 45, 33-38, 1974

Borkhuu, B., Snowfall at a high-elevation site: Comparisons of six measurement techniques, M.S. Thesis, Department of Atmospheric Science, University of Wyoming, 2009

Boudala, F.S., R.Rasmussen, G.A.Isaac, and B.Scott, Performance of hot plate for measureing solid precipitation in complex terrain during the 2010 Vancouver Winter Olympics, J. Atmos.Oceanic Technol., 31, 437-446, 2014

Brandes, E.A., K. Ikeda, G. Zhang, M. Schonhuber, and R.M. Rasmussen, A statistical and physical description of hydrometeor distributions in Colorado snowstorms using a video disdrometer, J. Appl. Meteor. Climatol., 46, 634- 650, 2007

Brock, F.V., and S.J. Richardson, Meteorological Measurement Systems, Oxford University Press, New York, 304 pp., 2001

Campbell, L.S., W.J. Steenburgh, P.G. Veals, T.W. Letcher, and J.R. Minder, Lake-Effect Mode and Precipitation Enhancement over the Tug Hill Plateau during OWLeS IOP2b, Mon. Wea. Rev., 144, 1729–1748, doi: 10.1175/MWR-D-15-0412.1, 2016

Currie, I., Snow in the rain gauge (photograph), Weather, 53, 100, 1989

Deshler, T., Corrections of surface particle probe measurements for the effects of aspiration, J. Atmos.Oceanic Technol., 5, 547–560, 1988

Goodison, B.E., P. Y. T. Louie, and D. Yang, WMO solid precipitation measurement intercomparison. WMO Tech. Doc. 872, 211 pp., 1998

Hansen, L.G. and B.W. Webb, Air jet impingement heat transfer from modified surfaces, International Journal of Heat and Mass Transfer, 36, 989-997, 1992

Hass, G., Filmed surfaces for reflecting optics, Journal of the Optical Society of America, 45, 945-952, 1955

Havilcek, L.L., and R.D. Crain, *Practical Statistics for the Physical Sciences*, American Chemical Society, 1988

Iribarne, J.V., and W.L.Godson, *Atmospheric Thermodynamics*, 2nd ed., Reidel, 1981

Jevons,W. S., On the deficiency of rain in an elevated rain gauge as caused by wind, London Edinburgh Dublin Philos. Mag., 22, 421–433, 1861

King, W.D., D.A. Parkin, and R.J. Handsworth, A hot-wire liquid water device having fully calculable response characteristics, J. Appl. Meteor., 17, 809-813, 1978

Kobus, C.J. and G.L.Wedekind, An experimental investigation into forced, natural and combined forced and natural convective heat transfer from stationary isothermal circular disks, Int. J. Heat Mass Transfer, 38, 3329-3339, 1995

Lempio, G.E., K. Bumke, and A. Macke, Measurement of solid precipitation with an optical disdrometer, Advances in Geosciences, 10, 91-97, 2007

Locatelli, J.D. and P.V.Hobbs, Fall speeds and masses of solid precipitation particles, J. Geophys. Res., 79, 2185-2197, 1974

Loffler-Mang, M. and J. Joss, An optical disdrometer for measuring size and velocity of hydrometeors, J. Atmos.Oceanic Technol., 17, 130-139, 2000

Lovblad, G., J.W. Erisman, and D. Fowler, Deposition monitoring. Models and Methods for the Quantification of Atmospheric Input to Ecosystems, Chapter 3, The Nordic Council of Ministers, 37-41, 1993

Nespor, V., and B. Servuk, Estimation of wind-induced error of rainfall gauge measurements using a numerical simulation, J. Atmos.Oceanic Technol., 16, 450-464, 1999

Panofsky, H.A. and J.A.Dutton, *Atmospheric Turbulence*, Wiley-Interscience, New York, pp. 397, 1984

Rasmussen, R.M., J. Hallett, R. Purcell, S.D. Landolt, and J. Cole, The hotplate precipitation gauge, J. Atmos.Oceanic Technol., 28, 148-164, 2011

Rasmussen, R., B. Baker, J. Kochendorfer, T. Meyers, S. Landolt, A.P. Fischer, J. Black, J.M. Theriault, P. Kucera, D. Gochis, C. Smith, R. Nitu, M. Hall, K, Ikeda, and E. Gutmann, How well are we measuring snow?, Bull. Amer. Meteor. Soc., 93, 811-829, 2012

Rogers, R.R. and M.K. Yau, *A Short Course in Cloud Physics*, 3rd ed. Permagon Press, 304 pp., 1989

Steenburgh, J., L.Campbell, and P. Veals, North Redfield Snow Study Station, http://data.eol.ucar.edu/datafile/nph-get/382.023/Redfield_met_stn_readme.pdf, 2014

Stickel, J., B.Maloney, C.Pape and D.Burkheimer, Evaluation of the hotplate snow gauge, Center for Transportation Research and Education, Iowa State University, Aurora Project 2004-01, 2005

Thériault, J.M, R.Rasmussen, K.Ikeda, and S.Landolt, Dependence of snow gauge collection efficiency on snowflake characteristics, J. Appl. Meteor. Climatol., 745-762, 2012

Warnick, C.C., Rime ice and snow capping on high altitude precipitation gages, Proceedings of the 25th Annual Western Snow Conference, Santa Barbara, California, Western Snow Conference, 24-34, 1957

Weast, R.C., Ed.,Handbook of Chemistry and Physics, 56th ed, Chemical Rubber Company, 2350 pp., 1975

Wettlaufer, A., A fully compensated algorithm for the hotplate precipitation sensor, M.S. Thesis, Department of Atmospheric Science, University of Wyoming, 2013

Wolfe, J.P., and J.R.Snider, A Relationship between Reflectivity and Snow Rate for a High-Altitude S-Band Radar, J. Appl. Meteor. Climatol., 51, 1111–1128, 2012

YES, INC., TPS-3100 Total Precipitation Sensor, Installation and User Guide, Version 2.0, Rev M, 43 pp., 2011

Young, H.D., *Statistical Treatment of Experimental Data*, McGraw-Hill Book Company, pp. 172, 1962

Figure 1 – The Yankee Environmental Systems TPS-3100 Total Precipitation Sensor with longwave and shortwave radiation sensors.

Figure 2 – Picture taken during indoor testing showing a hotplate's precipitation sensor positioned between top and bottom painted-steel sheets.

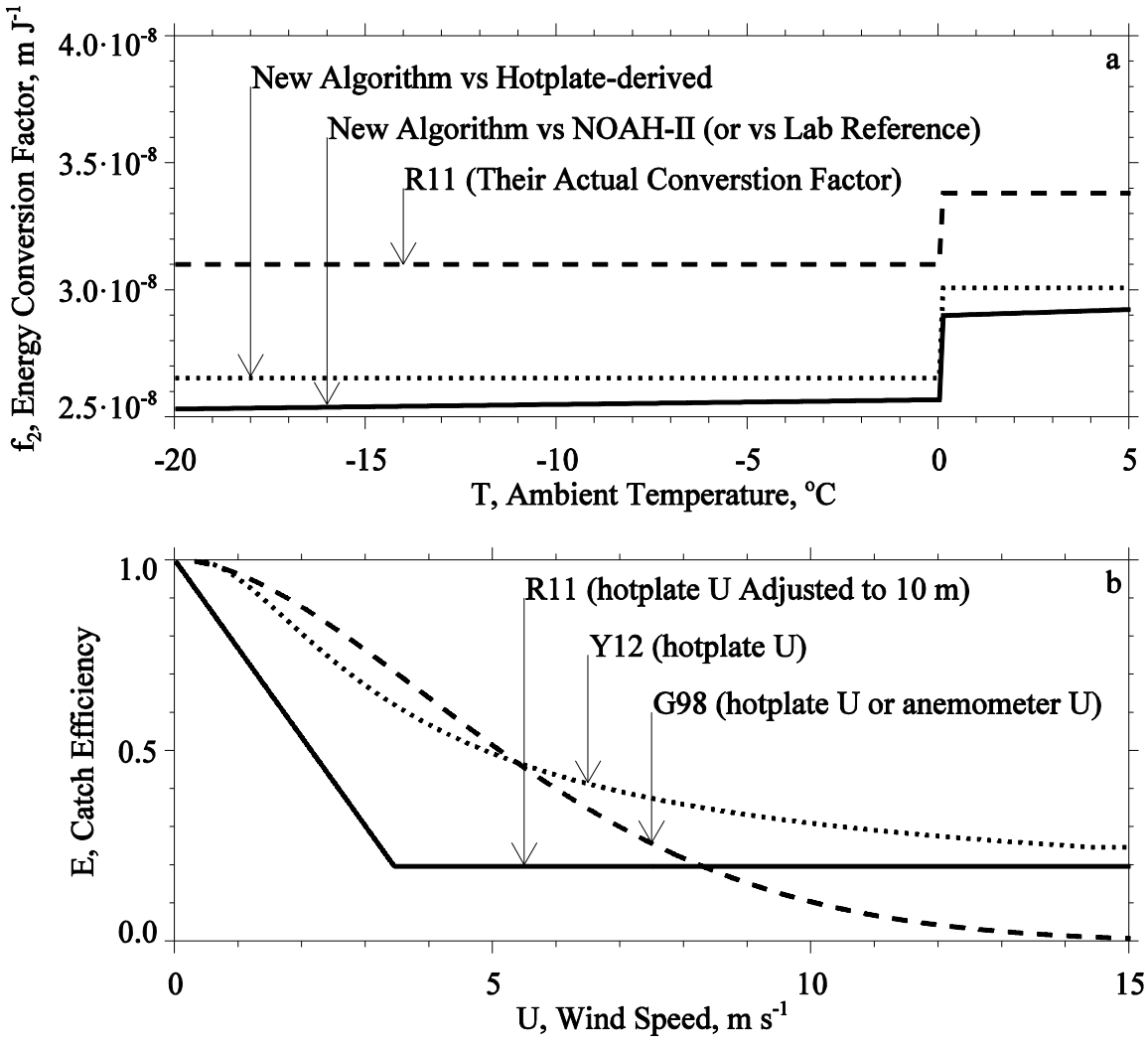

Figure 3 – a) Electrical-to-precipitation conversion factors vs ambient temperature assuming snow at $T < 0$ °C and rain at $T > 0$ °C. See text for details. b) Snow particle catch efficiency vs wind speed using the R11, Y12, and G98 formulations discussed in the text.

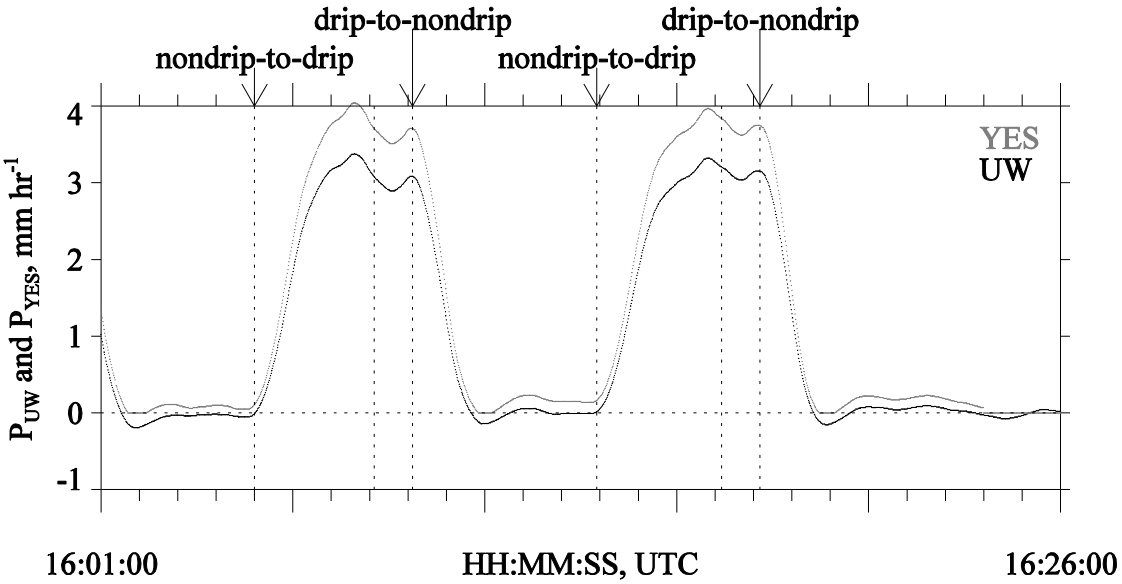

Figure 4 – Precipitation rates, derived using the UW and YES algorithms, plotted vs time. Dashed vertical lines illustrate nondrip-to-drip transitions, drip-to-nondrip transitions, and one-minute precipitation averaging intervals. In this figure, the one-minute averaging intervals are ~ 16:08 to ~ 16:09 UTC and ~ 16:17 to ~ 16:18 UTC. Measurements are from the UW hotplate operating indoors on 20120229. The UW/GLE calibration constants (Table 3) and an f_2 derived with the second of two methods (section 3.8) were applied in the UW algorithm.

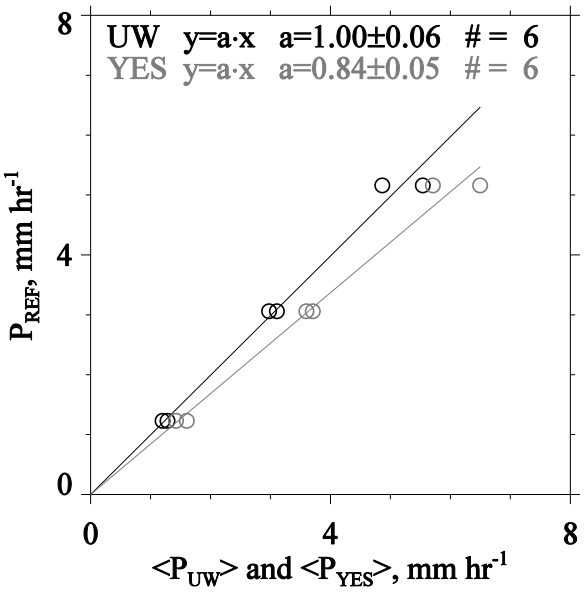

Figure 5 - Reference precipitation rate vs time-averaged P_{UW} and P_{YES}. Measurements are from the UW hotplate operating indoors on 20120229. The UW/GLE calibration constants (Table 3) and an f_2 derived with the second of two methods (section 3.8) were applied in the UW algorithm. Regression lines were forced through the origin and x deviations (horizontal departures of data from regression line) were used as the basis for the least squares criterion of best fit (Young, 1962). Standard deviations on the fitted ratios (confidence intervals) were derived using Student's t-distribution at the 95% level (Havilcek and Crain, 1988).

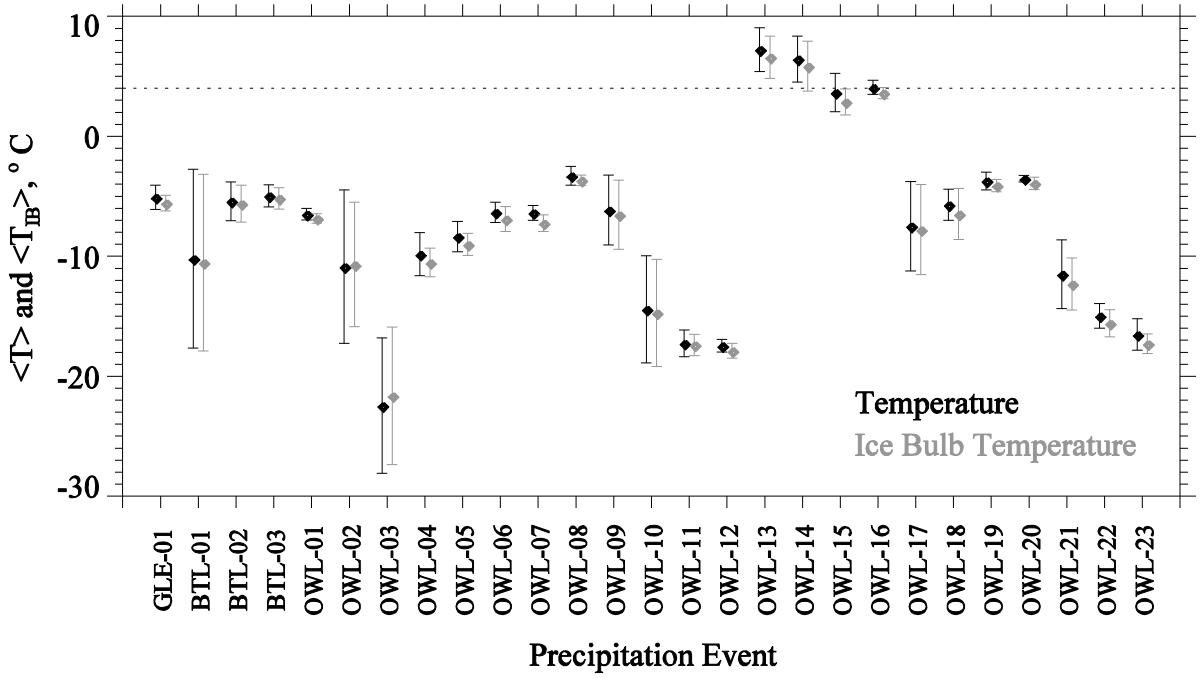

Figure 6 – Event-averaged ambient temperature (<*T*>) and event-averaged ambient ice bulb temperature (<T_{IB}>). The abscissa shows the 27 precipitation events in the order presented in Table 5. Error bars are ± 2 standard deviations. The dashed horizontal line is drawn at +4 ºC.

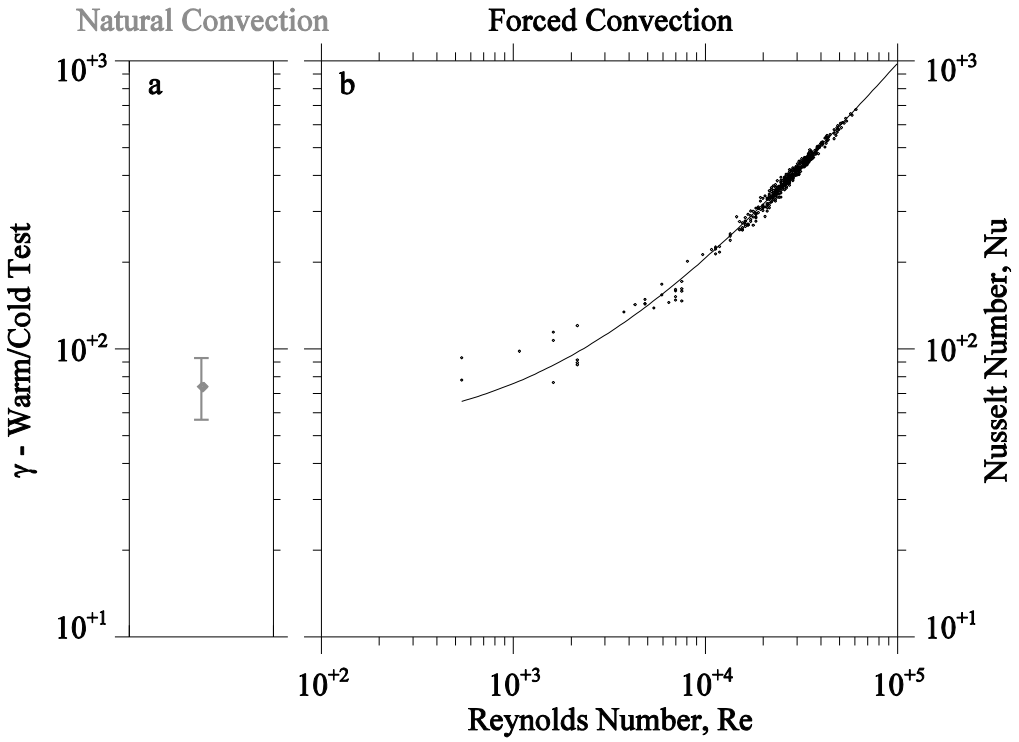

Figure 7 – a) γ from the warm-cold test summarized in the second row of Table 3. Error limits were derived by perturbing $Q_{top,w}$ (i.e., the value acquired in the warm test) by ± 0.5 W and repeating the analysis based on Eq. 7a - b. b) *Nu* vs *Re* scatterplot and fit curve for the UW hotplate at the GLE site. For clarity, only every fortieth *Nu*-*Re* data pair is plotted. The minimum *Re* plotted (data and fit function) corresponds to the minimum *U* reported in the UHP file (0.1 m s^{-1}). The measurement interval is 20120402 04:00 UTC to 20120402 09:00 UTC at the GLE site. The UW/GLE T_h (Table 3) was applied in the data analysis.

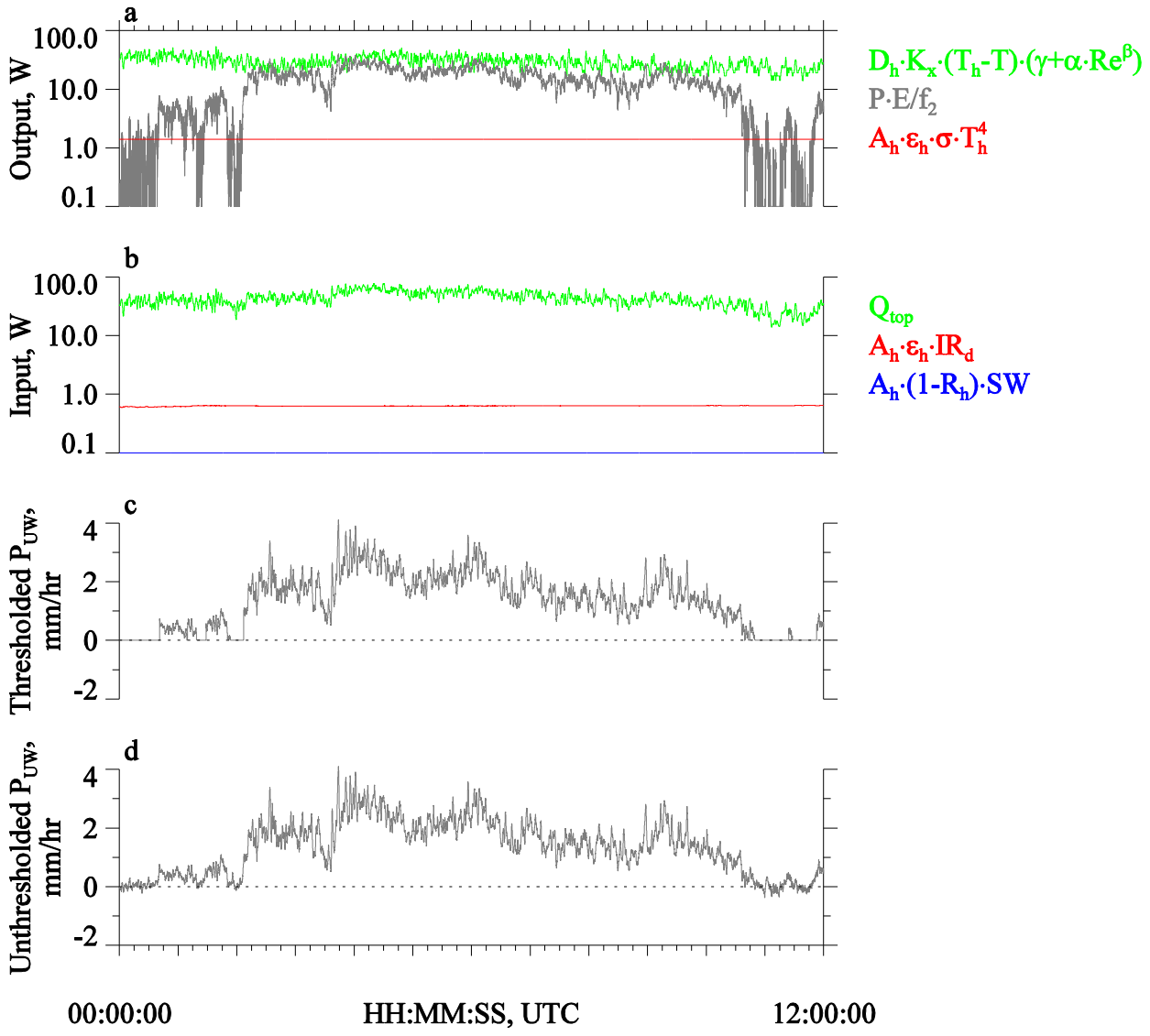

Figure 8 – Hotplate properties during rain (event = OWL-15). Because this event classifies as rain, $E = 1$ was applied in the UW algorithm. a) Budget output terms (Eq. 3); i.e., the sensible, latent, and longwave outputs. b) Budget input terms (Eq. 3); i.e., top plate, longwave, and shortwave inputs. The shortwave term is zero for this nighttime example, but is set to 0.1 W in the plot. c) Thresholded precipitation rate. d) Unthresholded precipitation rate.

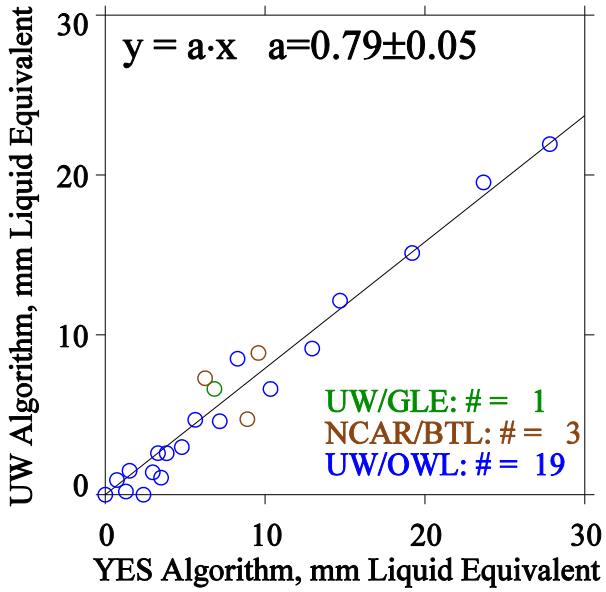

Figure 9 – Snow accumulations derived using the UW algorithm vs snow accumulations derived using the YES algorithm. Both the Y12 catch efficiency function and an f_2 derived with the first of two methods discussed in section 3.8 were applied in the UW algorithm. The regression line was forced through the origin and *y* deviations (vertical departures of data from regression line) were used as the basis for the least squares criterion of best fit (Young, 1962). The standard deviation on the fitted ratio (confidence interval) was derived using Student's t-distribution at the 95% level (Havilcek and Crain, 1988).

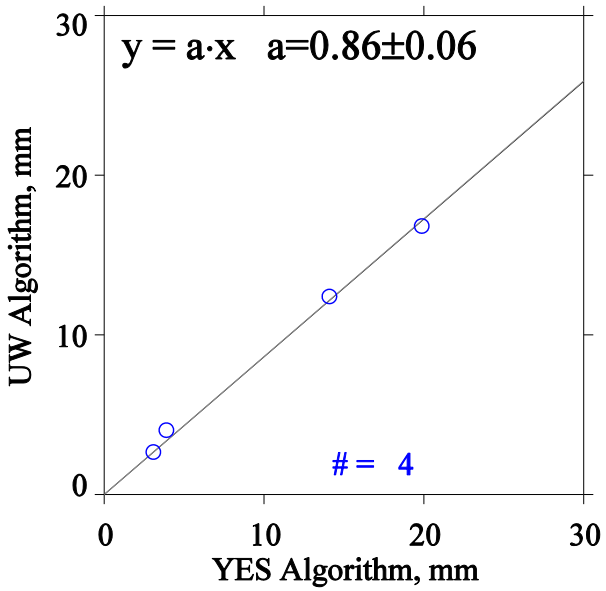

Figure 10 – Rain accumulations derived using the UW algorithm vs rain accumulations derived using the YES algorithm. An f_2 derived with the first of two methods discussed in section 3.8 was applied in the UW algorithm. The regression line was forced through the origin and *y* deviations (vertical departures of data from regression line) were used as the basis for the least squares criterion of best fit (Young, 1962). The standard deviation on the fitted ratio (confidence intervals) was derived using Student's t-distribution at the 95% level (Havilcek and Crain, 1988).

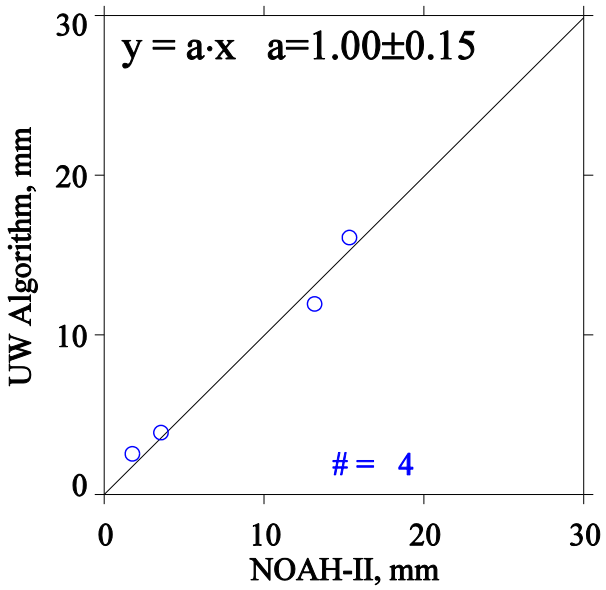

Figure 11 –Rain accumulations derived using the UW algorithm vs rain accumulations from the NOAH-II gauge. An f_2 derived with the second of two methods discussed in section 3.8 was applied in the UW algorithm. The regression line was forced through the origin and y deviations (vertical departures of data from regression line) were used as the basis for the least squares criterion of best fit (Young, 1962). The standard deviation on the fitted ratio (confidence intervals) was derived using Student's t-distribution at the 95% level (Havilcek and Crain, 1988).

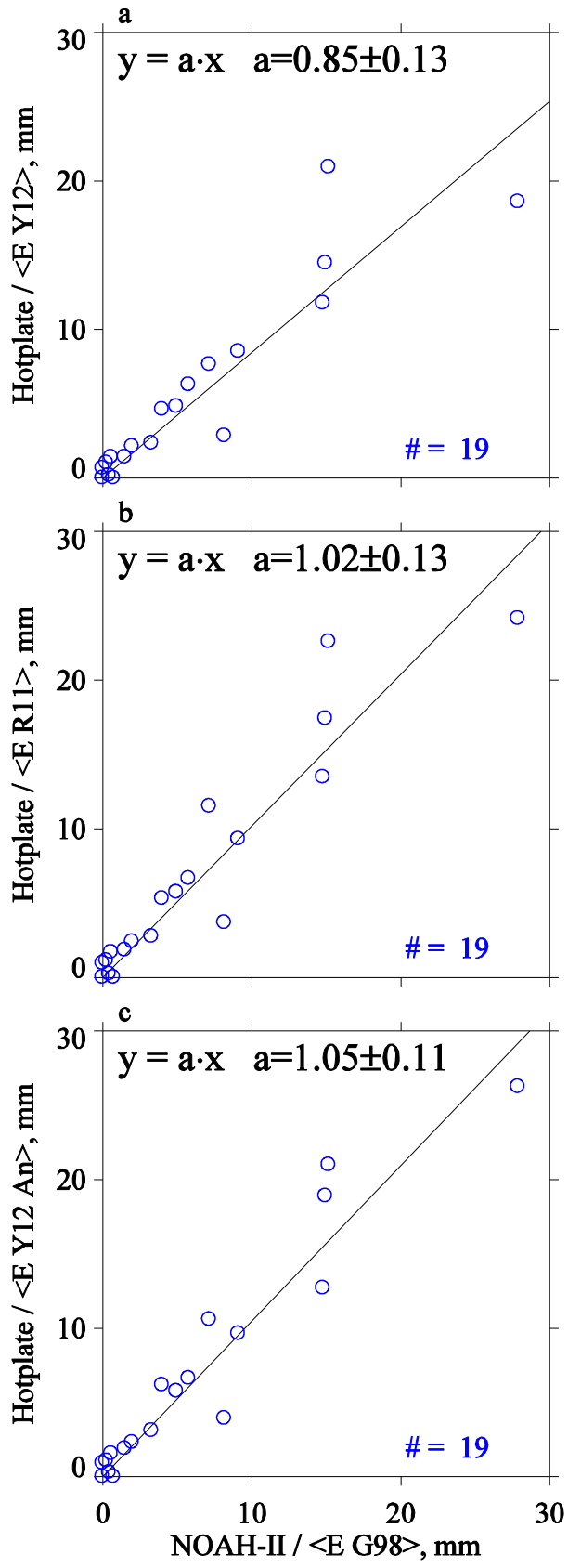
a
y = a·x a=0.85±0.13
Hotplate / <E Y12>, mm
= 19
b
y = a·x a=1.02±0.13
Hotplate / <E R11>, mm
= 19
c
y = a·x a=1.05±0.11
Hotplate / <E Y12 An>, mm
= 19
0
10
20
30
NOAH-II / <E G98>, mm

963 Figure 12 – UW hotplate and NOAH-II measurements of snow (liquid-equivalent
964 accumulations, not corrected for inefficient catch, divided by an event-averaged snow particle
965 catch efficiency) at OWL. An f_2 derived with the second of two methods discussed in section 3.8
966 was applied in the UW algorithm. Regression lines were forced through the origin and *y*
967 deviations (vertical departures of data from regression line) were used as the basis for the least
968 squares criterion of best fit (Young, 1962). The standard deviations on the fitted ratios
969 (confidence intervals) were derived using Student's t-distribution at the 95% level (Havilcek and
970 Crain, 1988).

971

972 **Table 1 – Hotplate Data Files**

Recorded Variable [a], units	File UHP	File SHP	Symbol
Unix Time, s	✓	✓	
Liquid-equivalent Precipitation Rate, mm hr^{-1}	✓		P_{YES}
Accumulated Liquid-equivalent Precipitation, mm	✓		
Ambient Temperature, ^{o}C	✓	✓	T
Enclosure Temperature, ^{o}C	✓	✓	
Wind Speed, m s^{-1}	✓		U
Downwelling Shortwave Flux, W m^{-2}	✓	✓	SW
Longwave Radiation Measurement, W m^{-2}	✓	✓	M_{IR}
Barometric Pressure, hPa	✓	✓	p [b]
Relative Humidity Sensor Temperature, ^{o}C	✓	✓	
Relative Humidity, %	✓	✓	RH
Top Plate Voltage, V		✓	
Bottom Plate Voltage, V		✓	
Top Plate Current, A		✓	
Bottom Plate Current, A		✓	
Top Plate Resistance, Ω		✓	
Bottom Plate Resistance, Ω		✓	
Top Plate Power, W		✓	Q_{top}
Bottom Plate Power, W		✓	Q_{bot}
Radiation Sensors' Temperature, ^{o}C		✓	

973

974

975 [a] With the exception of Unix time, all recorded variables are 60-s running averages, sampled at 1 Hz
976 (YES, 2011)

977 [b] Although pressure is a recorded variable, the pressure used in the UW algorithm (p_x; section 3.7 and
978 Appendix) is the standard-atmosphere pressure at the altitude of the measurement

Table 2 – Field Sites, Site Location, Vegetation at the Site, Gauge Location, Number of Events, and Event Type

Site Abbreviation Site Reference Hotplate	Site Location	Height of Vegetation, m AGL	Gauge Location at Site	Precipitation Events
GLE Wettlaufer (2013) UW	SE Wyoming 106.240 °W 41.3665 °N 3190 m MSL	10 to 20 m	Hotplate: 27 m AGL on top deck of a meteorological tower [a] NOAH-II: 3 m AGL (clearing in conifer forest 80 m SE of tower)	1 Snow
BTL Wettlaufer (2013) NCAR	SE Wyoming 106.975 °W 41.1558 °N 3010 m MSL	10 to 20 m	Clearing in conifer forest Hotplate: 3 m AGL NOAH-II: 3 m AGL	3 Snow
OWL Steenburgh et al. (2014) UW	NW New York 75.8771 °W 43.6245 °N 385 m MSL	2 to 5 m	Clearing in deciduous brush and deciduous trees Hotplate: 1.7 m AGL [b] and 2.5 m AGL [c] NOAH-II: 2.5 m AGL	4 Rain 19 Snow

[a] This is the Brooklyn Lake, Wyoming AmeriFlux Tower; AmeriFlux is a network of sites that measure energy and trace-gas transfers.

[b] First 7 of 23 OWL precipitation events (Date < 20131217)

[c] Last 16 of 23 OWL precipitation events (Date > 20131217)

Table 3 – Summary of Warm-cold Tests

Indoor Calibration (Warm-cold Tests)			
Year	Hotplate/Field Site	T_h, ^oC	γ
2012	NCAR/BTL	42.2 ± 7.4 [a]	106. ± 15.1 [a]
2012 - 2013	UW/GLE	52.2 ± 15.7	74.8 ± 18.1
2013 - 2015	UW/OWL	66.5 ± 7.8	57.8 ± 7.7

[a] Error limits derived by perturbing $Q_{top,w}$ (i.e., the value acquired in the warm test) by ± 0.5 W and repeating the analysis based on Eq. 7a - b.

Table 4 – Summary of Drip Tests

Indoor Calibration (Drip Tests)				
Year	Hotplate/Field Site	P_{REF} vs $<P_{UW}>$ ratio [a]	P_{REF} vs $<P_{YES}>$ ratio [a]	# [b]
2012	NCAR/BTL	0.99 ± 0.02	0.81 ± 0.03	6
2012 - 2013	UW/GLE	1.00 ± 0.06	0.84 ± 0.05	6
2013 - 2015	UW/OWL	0.97 ± 0.04	0.79 ± 0.03	6

[a] Ratios were derived as the slope of a regression lines forced through the origin. The *x* deviations (horizontal departures of data from regression line) were used as the basis for the least squares criterion of best fit (Young, 1962). Standard deviations on the fitted ratios (confidence intervals) were derived using Student's t-distribution at the 95% level (Havilcek and Crain, 1988).

[b] # = number of tests.

Table 5 – Precipitation Events

Precipitation Event	Start Date, YYYYMMDD UTC	Start Time, HH:MM UTC	End Time HH:MM UTC	<T> [a], °C	<T_{IB}> [b], °C	<U> [c], m s^{-1}	UW [d], mm	YES [d], mm	<E Y12> [e]	<E Y12 An> [f]	<E R11> [g]	NOAH-II [d], mm	<E G98> [h]
GLE-01	20120414	0:00	13:00	-5.1	-5.6	1.8	5.6	6.0	0.84	NA [i]	NAP [j]	7.3	0.89
BTL-01	20120116	11:00	1:00	-10.2	-10.5	2.0	3.8	7.5	0.80	NA	NAP	8.0	0.87
BTL-02	20120119	8:00	18:00	-5.4	-5.6	4.3	3.8	3.4	0.55	NA	NAP	1.0	0.60
BTL-03	20120120	7:00	18:00	-5.0	-5.2	2.4	6.3	7.1	0.75	NA	NAP	8.2	0.83
OWL-01	20131211	18:00	0:00	-6.5	-6.9	1.4	16.9	21.5	0.91	0.64	0.70	20.0	0.72
OWL-02	20131212	0:00	6:00	-10.9	-10.7	0.4	1.0	3.5	0.99	0.94	0.90	0.3	0.96
OWL-03	20131212	6:00	12:00	-22.5	-21.6	0.3	0.0	2.4	1.00	1.00	0.93	0.0	1.00
OWL-04	20131212	18:00	0:00	-9.8	-10.5	1.3	0.2	1.2	0.90	0.53	0.67	0.3	0.57
OWL-05	20131213	6:00	12:00	-8.4	-9.0	0.9	13.9	18.5	0.96	0.73	0.80	12.1	0.81
OWL-06	20131215	19:45	0:00	-6.3	-6.9	0.9	1.3	2.9	0.94	0.85	0.78	0.5	0.88
OWL-07	20131216	0:00	6:00	-6.4	-7.3	0.3	20.9	27.8	1.00	1.00	0.93	15.2	1.00
OWL-08	20131218	18:00	0:00	-3.3	-3.7	1.5	10.4	13.2	0.88	0.82	0.77	12.9	0.87
OWL-09	20140106	18:00	0:00	-6.2	-6.5	3.9	4.5	4.6	0.58	0.42	0.39	2.5	0.35
OWL-10	20140107	0:00	6:00	-14.4	-14.7	3.8	0.4	0.3	0.60	0.44	0.42	0.0	0.38
OWL-11	20140107	6:00	12:00	-17.3	-17.4	3.0	1.9	3.3	0.67	0.49	0.52	4.0	0.49
OWL-12	20140107	18:00	0:00	-17.5	-17.9	3.9	0.0	0.0	0.58	0.42	0.39	0.3	0.35
OWL-13	20140111	15:45	21:00	7.2	6.6	1.1	11.9	14.1	1.00	1.00	1.00	13.2	1.00
OWL-14	20140111	23:00	2:00	6.4	5.8	2.4	3.9	3.9	1.00	1.00	1.00	3.5	1.00
OWL-15	20140114	0:00	12:00	3.7	2.9	0.9	16.1	19.9	1.00	1.00	1.00	15.3	1.00
OWL-16	20140114	12:45	15:45	4.1	3.6	1.2	2.6	3.1	1.00	1.00	1.00	1.8	1.00
OWL-17	20140119	0:00	12:00	-7.5	-7.8	1.3	1.9	3.3	0.91	0.84	0.81	1.8	0.88
OWL-18	20140119	18:00	0:00	-5.7	-6.5	1.9	1.9	2.6	0.81	0.61	0.69	2.3	0.69
OWL-19	20140120	0:00	2:00	-3.7	-4.1	3.1	0.9	1.0	0.67	0.50	0.52	0.8	0.51
OWL-20	20140120	2:00	12:00	-3.5	-3.9	2.1	3.8	4.8	0.78	0.66	0.66	3.5	0.72
OWL-21	20140127	18:00	0:00	-11.5	-12.3	1.7	4.0	6.6	0.86	0.65	0.75	2.8	0.69
OWL-22	20140128	0:00	6:00	-15.0	-15.6	0.4	6.3	10.3	1.00	0.95	0.94	5.6	0.96
OWL-23	20140128	6:00	12:00	-16.5	-17.3	0.9	8.0	12.1	0.94	0.83	0.86	8.1	0.88

[a] Event-averaged ambient temperature
[b] Event-averaged ice bulb temperature
[c] Event-averaged hotplate *U*
[d] Liquid-equivalent precipitation amount not corrected for inefficient catch (UW values are computed with an f_2 derived with the second of two methods discussed in section 3.8)
[e] Event-averaged snow particle catch efficiency derived using Y12 and the hotplate *U*
[f] Event-averaged snow particle catch efficiency derived using Y12 and the anemometer *U*
[g] Event-averaged snow particle catch efficiency derived using R11 and hotplate *U* adjusted to 10 m AGL
[h] Event-averaged snow particle catch efficiency derived using G98 and hotplate *U* (GLE and BTL) or anemometer *U* (GLE)
[i] NA = not available
[j] NAP = not applicable

Table 6 – Summary of Fitted *Nu*-*Re* Coefficients

Field Calibration (*Nu* - *Re* Coefficients)			
Hotplate/Field Site	γ	α	β
NCAR/BTL [a]	86.2	0.126	0.781
UW/GLE [b]	49.1	0.130	0.771
UW/OWL [c]	45.6	0.172	0.713

[a] NCAR hotplate; measurement interval 20120118 23:00 UTC to 20120119 5:00 UTC

[b] UW hotplate; measurement interval 20120402 04:00 UTC to 20120402 09:00 UTC

[c] UW hotplate; measurement interval 20140107 18:00 UTC to 20140108 08:00 UTC